Human Pathology 173 (2026) 106114

Contents lists available at ScienceDirect

Human Pathology

journal homepage: www.elsevier.com/locate/humpath

Spatially-resolved CD8$^+$ and CD34$^+$ computational immunohistochemistry indicators improve post-nephrectomy risk stratification in clear cell renal cell carcinoma

Mantas Fabijonavicius [a,d,*], Ausra Garnelyte [b], Dovile Zilenaite-Petrulaitiene [b,c], Allan Rasmusson [b,c], Julius Drachneris [b,c], Albertas Cekauskas [a,d], Feliksas Jankevicius [a,e], Arvydas Laurinavicius [b,c]

[a] Center of Urology, Vilnius University Hospital Santaros Klinikos, Vilnius, Lithuania
[b] National Center of Pathology, Affiliate of Vilnius University Hospital Santaros Klinikos, Vilnius, Lithuania
[c] Center for Digital Medicine, Translational Health Research Institute, Vilnius University, Vilnius, Lithuania
[d] Clinic of Gastroenterology, Nephrourology and Surgery, Institute of Clinical Medicine, Faculty of Medicine, Vilnius University, Vilnius, Lithuania
[e] National Cancer Institute, Vilnius, Lithuania

ARTICLE INFO

Keywords:
Clear cell renal cell carcinoma
CD8$^+$ cells
CD34
Tumor microenvironment
Spatial analysis
Prognostic biomarkers
Digital immunohistochemistry

ABSTRACT

Objectives: Clear cell renal cell carcinoma (ccRCC) is a heterogeneous tumor that may progress after nephrectomy as local or distant disease. The ccRCC tumor microenvironment (TME) hinges on two complementary pillars of immune response and angiogenesis. We aimed to assess if spatial CD8 and CD34 profiles at the tumor-stroma interface predict progression-free survival (PFS).

Methods: We retrospectively analyzed 214 ccRCC patients treated at Vilnius University Hospital Santaros Klinikos (2009 – 2019). Immunohistochemistry for CD8 and CD34 was performed on surgical tumor excision samples, and digital image analysis was performed to quantify cell densities and vessel areas relative to their spatial patterns within the tumor-stroma interface. The impact on PFS of CD8$^+$ immunogradient and CD34$^+$ area fraction was tested.

Results: Two prognostic models were developed: a Baseline model using variables available after surgery and a Disease-Course model additionally incorporating follow-up information. In the Baseline model, higher CD8_m_CM independently predicted shorter PFS (HR 3.24, $p = 0.001$), together with tumor size >4.95 cm and coagulative tumor necrosis, while female sex predicted longer PFS. In the Disease-Course model, local recurrence was the strongest adverse predictor (HR 17.69, $p < 0.001$), while both spatial biomarkers remained independently associated with PFS: higher CD8_m_CM predicted shorter PFS (HR 5.14, $p = 0.001$), whereas higher VAF_m_CM predicted longer PFS (HR 0.32, $p = 0.014$).

Conclusions: Spatial patterns of immune and vascular components at the tumor-stroma interface independently predict PFS in patients with ccRCC following nephrectomy and may improve current risk stratification schemes in both the immediate postoperative setting and during follow-up.

1. Introduction

Renal cell carcinoma (RCC) affects over 400,000 people worldwide annually, accounting for approximately 3% of all cancer diagnoses. Its highest prevalence is observed in Western countries, with a clear predominance in men [1]. Clear cell renal cell carcinoma (ccRCC), the most common subtype constituting 70 – 80% of RCC cases, is characterized by its histopathological and molecular heterogeneity, genetic variability, rich neovascularization, and often aggressive behavior [2]. Contemporary prognostic tools, encompassing tumor-node-metastasis (TNM) classification, stage and composite clinicopathological nomograms such as the UCLA Integrated Staging System (UISS) [3], the Memorial Sloan-Kettering Cancer Center (MSKCC) [4] and the Mayo Clinic Stage, Size, Grade, and Necrosis score (SSIGN) [5], provide only modest discrimination in the era of precision oncology [6–8]. Consequently, attention has shifted toward properties of the tumor microenvironment

* Corresponding author. Vilnius University Hospital Santaros Klinikos, Santariskiu st. 2, 08661, Vilnius, Lithuania.
E-mail address: m.fabijonavicius@santa.lt (M. Fabijonavicius).

https://doi.org/10.1016/j.humpath.2026.106114
Received 8 January 2026; Received in revised form 27 March 2026; Accepted 31 March 2026
Available online 1 April 2026

(TME) that could refine risk stratification and guide adjuvant therapy selection [9–12].

Among immune constituents of the TME, $CD8^+$ cytotoxic T-lymphocytes play a central role in antitumor immunity and in mediating the therapeutic effects of immune-checkpoint inhibitors (ICI) [12–14]. However, unlike in colorectal, breast, or lung carcinomas, where high $CD8^+$ cell densities indicate favorable outcomes, studies in ccRCC report variable results and somewhat paradoxical associations with poor prognosis [15–17]. The paradox likely stems from the spatial heterogeneity and functional exhaustion of these cells [18–21]. This variation has propelled digital Immunoscore initiatives that go beyond crude cell counts to capture the location and spatial distributions of immune cells across the tumor–stroma interface [22–24]. To make this concept actionable, standardized, spatially resolved readouts are required. Digital pathology now enables high-capacity, reproducible quantification of $CD8^+$ spatial patterns that is suitable for large tissue samples and patient cohorts.

Angiogenesis represents the second major pillar of the ccRCC TME. Loss of von Hippel–Lindau (VHL) function stabilizes hypoxia-inducible factor (HIF) and drives vascular endothelial growth factor (VEGF)-dependent neovascularization. Accordingly, VEGF and the mammalian target of rapamycin (mTOR) inhibitors remain therapeutic backbones when ICIs fail [25]. Microvessel density (MVD), usually assessed with pan-endothelial markers such as CD31, CD34, or von Willebrand factor (VWF), is the most common surrogate for angiogenesis in solid tumors and correlates with poor outcomes in prostate, breast, lung, and melanoma [26]. In ccRCC, however, meta-analyses have found MVD alone unreliable [27]. Similarly, endothelial-cell proliferation indices and microvessel area (MVA) have yielded conflicting results [28,29]. These discrepancies may stem from the fact that pan-endothelial stains capture both quiescent and activated vessels, disregarding vessel maturity and their spatial distribution within the complex tumor-stroma landscape. CD34, although traditionally considered a pan-endothelial marker, is preferentially retained on pericytes and maturing capillaries, providing a read-out of vessel-architectural remodeling in ccRCC [30]. Predominance of differentiated $CD34^+$ microvessels within the tumor, rather than at the periphery of the tumor, is consistent with a more mature and better-perfused TME [28,31,32], whereas edge-skewed angiogenesis at the invasive front has been associated with worse outcomes in ccRCC [33].

Taken together, the immune and vascular components of the ccRCC TME may exert distinct, topography-dependent effects on clinical outcome. We therefore hypothesized that integrating spatial density gradients of both $CD8^+$ T-cells and $CD34^+$ vessels with established clinicopathological variables could enhance risk stratification of the patients after nephrectomy. In this study, we assessed the prognostic value of computational, spatially-resolved $CD8^+$ and $CD34^+$ immunohistochemistry (IHC) biomarkers obtained from the tumor-stroma interface in surgical excision samples of 214 ccRCC patients.

2. Materials and methods

2.1. Study population

Our study used a retrospective cohort of 245 patients (146 males and 99 females) who underwent surgical treatment for ccRCC at Vilnius University Hospital Santaros Klinikos (Vilnius, Lithuania) between 2009 and 2019. Histopathological evaluation of the surgical specimens was performed at the National Center of Pathology, an affiliate of the Vilnius University Hospital Santaros Klinikos (Vilnius, Lithuania). Clinical and pathological data were retrospectively collected with approval from the Vilnius Regional Biomedical Research Ethics Committee (permit No. 2024/9-1600-1062). To maintain the patient cohort focused on localized ccRCC, 24 patients were excluded due to the presence of metastases prior to surgical intervention. Additionally, 3 cases with sarcomatoid differentiation and 4 cases with lymph node metastases were excluded from further analyses to avoid potential bias introduced by the highly aggressive nature of these tumors. Finally, 214 ccRCC patients were included in the analysis. The median post-surgery follow-up time was 81 (range 3 to 120) months calculated from the time of pathologically proven diagnosis to the last follow-up date or radiologically proven statement of disease progression (defined as one or more distant metastases). PFS times were censored after 10 years to minimize potential outliers and long-term survivor bias. Clinicopathological characteristics and follow-up data for the patient cohort are summarized in Table 1.

2.2. Immunohistochemistry and imaging

A pathologist (AG) reviewed archival hematoxylin and eosin-stained (H&E) slides and selected the most representative formalin-fixed paraffin-embedded (FFPE) tissue block for each patient (one block per case). The selected FFPE block was required to contain both tumor tissue of ccRCC along with adjacent kidney parenchyma (N = 214) (Fig. 1A) The selected samples were cut at 3 μm thickness, mounted onto positively charged slides, and stained with a CD8 antibody (Agilent Dako, clone C8/144B, dilution 1:100, Denmark) and a CD34 antibody (Agilent Dako, Monoclonal Mouse Anti-Human CD34 Class II, Clone QBEnd 10,

Table 1
Clinical, pathological, and follow-up characteristics.

Characteristic	Value
Patient cohort	214 (100%)
Age, years	
Mean (range)	62.63 (27 – 88)
Median	62
Gender	
Male	122
Female	92
PFS time, months	
Median	34.83 (5.13 – 112.43)
Disease progression	25.95
	38
Multiple renal carcinomas	
No	198
Yes	16
Surgery type	
Radical nephrectomy	114
Partial nephrectomy	100
Largest tumor dimension, cm	
Mean (range)	4.42 (0.7 – 18)
Median	3.95
Local recurrences during follow-up period	
No	203
Yes	11
Grade ISUP/WHO	
1	7
2	110
3	95
4	2
Coagulative tumor necrosis status	
Negative	189
Positive	25
Lymphovascular invasion (LVI) status	
Negative	175
Positive	39
pT stage	
1a	95
1b	45
2a	4
2b	1
3a	68
3b	0
4	1
Resection margin	
R0	199
R1	15

* PFS – progression-free survival; ISUP/WHO – the International Society of Urologic Pathologists/World Health Organization grading system.

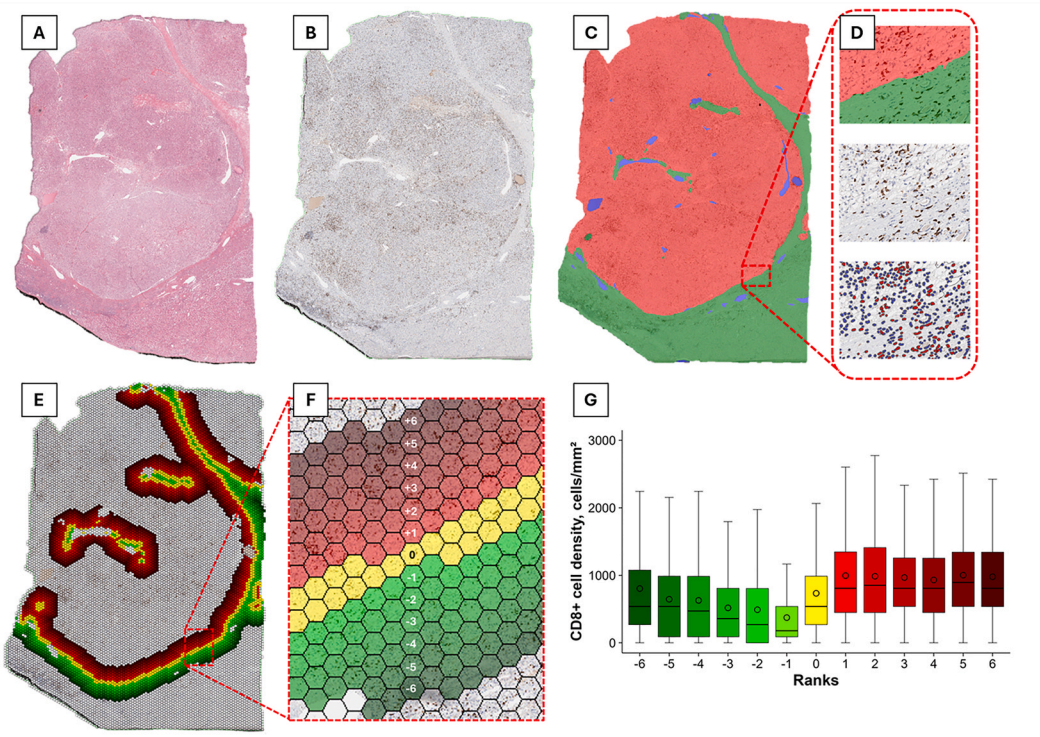

Fig. 1. Study workflow to assess CD8$^+$ cell density profiles at the tumor-stroma interface: (**A**) Low-magnification Hematoxylin and Eosin-stained section of a representative ccRCC tissue; (**B**) Corresponding CD8 immunohistochemistry (IHC) slide used for downstream image analysis; (**C**) HALO®AI ccRCC tissue classifier output identifying tumor (red), stroma (green), and background (blue); (**D**) Zoomed region of interest: top, tissue-class masks; middle, native CD8 IHC; bottom, IHC nuclear segmentation with CD8-positive cells in red and CD8-negative cells in blue; (**E**) Hexagonal grid overlaid on the CD8 IHC slide, highlighting the tumor-stroma interface zone; (**F**) Enlarged view of the ranked hexagon grid illustrating the scale from −6 (stroma, green) to +6 (intratumor, red); (**G**) Boxplots for the corresponding case (A-F) of hexagon-level CD8$^+$ cell densities across ranked bins of the tumor–stroma interface (ranks −6 to +6). The thick horizontal line denotes the median; the hollow circle denotes the mean; the yellow box marks the tumor edge (rank 0); background shading indicates stroma (green) and tumor (red). (For interpretation of the references to color in this figure legend, the reader is referred to the Web version of this article.)

concentrate, Denmark) using a Roche Ventana BenchMark ULTRA automated stainer (Ventana Medical Systems, Oro Valley, AZ, USA). The staining process utilized the ultraView Universal DAB Detection kit (Ventana Medical Systems, Oro Valley, AZ, USA) for signal visualization. All CD8 and CD34 IHC-stained slides were scanned at 20x magnification (0.5 µm per pixel) using an Aperio® AT2 DX scanner (Leica Aperio Technologies, Vista, CA, USA).

2.3. Image analysis

The HALO® AI platform version 3.6.4134 (Indica Labs, USA) was used to classify the tissue compartments. The DenseNet v2 classifier was trained with manual annotations provided by the pathologist (AG), categorizing regions as tumor, stroma and background (Fig. 1C and D; Fig. 2B). The background class was used to exclude areas of necrosis, hemorrhage, and cysts, which could interfere with spatial analysis. All images were subsequently reviewed by the pathologist (AG), and tissue areas smaller than 1000 µm^2 were excluded using the HALO® AI minimum object size filter to mitigate noise resulting from small, inaccurately identified foci. Following the tissue classification, CD8$^+$ cell segmentation was performed utilizing the HALO® Multiplex IHC algorithm (version 3.1.4, Indica Labs, USA) (Fig. 1D).

Hexagonal tiling of the digital image analysis (DIA) outputs was performed to compute tumor-stroma interface zone immunogradient indicators (quantitative metrics that capture immune cell densities across the tumor-stroma interface) as reported by Rasmusson et al. [21]. A hexagonal grid with a side length of 260 pixels (65 µm) was used for this study. Briefly, a hexagonal grid overlay was randomly positioned to generate subsamples of DIA results (Fig. 1E). Hexagons marking the boundary between the ccRCC and adjacent kidney tissue (stroma) were identified based on an abrupt changes in the percentage of tissue-class area across the grid. Tiles were then ranked based on their position within the tissue. Hexagons marking tumor edge (TE) were assigned a rank 0, and hexagons signifying tumor tissue were assigned a positive rank corresponding to their distances from the nearest TE (+1, +2, +3, etc.), while the stromal hexagons were assigned negative ranks (−1, −2, −3, etc.) based on the same distance principle. Various settings of tumor-stroma interface zone widths were tested to evaluate their effects on indicator performance. For CD8, candidate interface-zone widths were evaluated for technical feasibility and stability of rank-wise sampling across the cohort. The final width of 13 hexagonal ranks (TE plus six ranks into tumor and six into stroma) was selected because it provided balanced coverage on both sides of the boundary while minimizing missingness in distal ranks. Wider interface zones led to progressive loss of analysable hexagons and reduced cohort representativeness at distal ranks, whereas narrower zones provided less stable sampling of the interface. This definition was fixed before outcome modelling and used for all subsequent CD8 analyses (Fig. 1E–G).

For CD34, the tumor compartment mask generated by the tissue classifier was used to restrict analysis to intratumoral regions (Fig. 2C). Within this compartment, a supervised HALO® AI classifier was trained to identify CD34-positive microvascular profiles (Fig. 2C and D). To avoid artificial fragmentation of elongated vessels that occur with object-based segmentation, tumor vascularity was quantified by area fraction rather than by vessel counts. CD34 indicators were computed across tumor-side ranks 0 to +6 of the interface zone to minimize variability attributable to stromal glomeruli and large vessels, while matching the CD8 configuration to ensure methodological consistency and reproducibility (Fig. 2E and F).

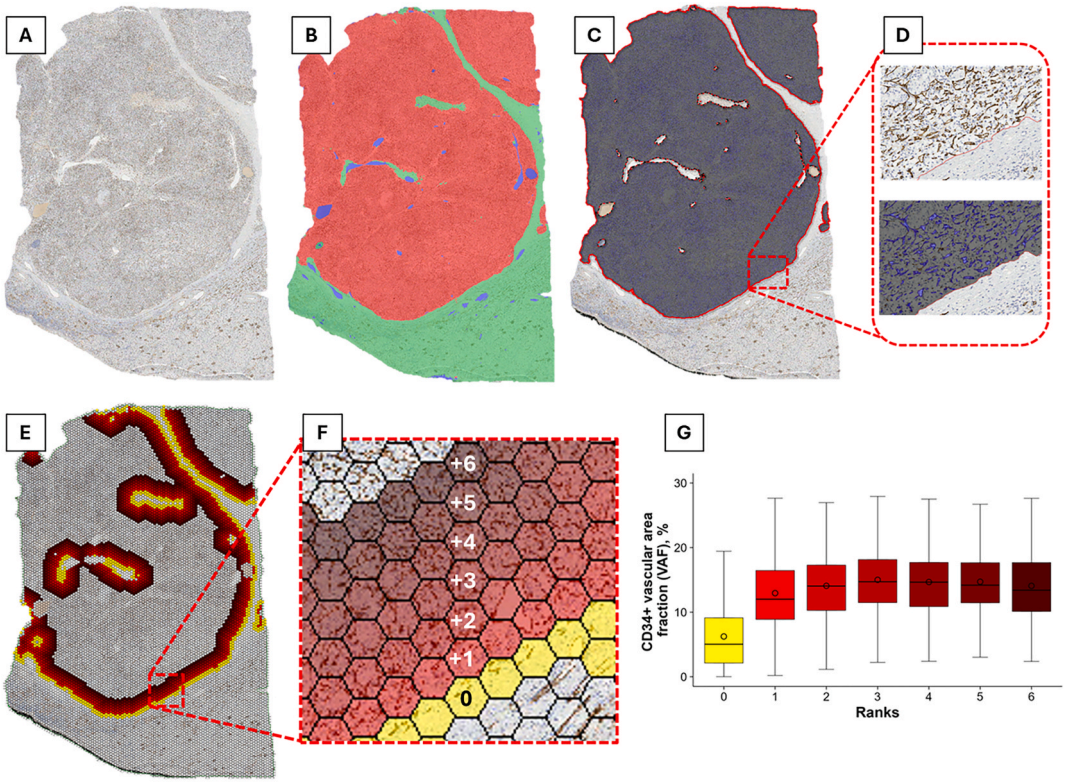

Fig. 2. Workflow to quantify intratumoral vascularity from CD34 IHC at the tumor–stroma interface: (**A**) Whole-slide CD34 immunohistochemistry (IHC) of a representative ccRCC case; (**B**) HALO® AI tissue classifier identifying tumor (red), stroma (green), and background/excluded areas (blue); (**C**) Tumor-only analysis mask overlaid on the CD34 slide with the tumor boundary traced in red; stroma regions are excluded; (**D**) Zoomed region of interest: top, native CD34 IHC; bottom, automated microvessel segmentation with vessel overlays in blue used to compute vessel area fraction; (**E**) Hexagonal tiling with automatic detection of the tumor–stroma interface with tiles inside the tumor ranked relative to it; tiles in the stroma region were ignored for CD34; (**F**) Enlarged view of the ranked intratumoral grid illustrating the distance scale from 0 at the edge to +6 deeper within the tumor, from which rank-wise vascular area fractions and the vascular center-of-mass are derived; (**G**) Boxplots for the corresponding case (A–F) of hexagon-level $CD34^+$ vascular area fraction (VAF, %) across ranks 0 to +6 of the tumor–stroma interface. The thick horizontal line denotes the median; the hollow circle denotes the mean; the yellow box marks the tumor edge (rank 0); background shading indicates tumor (red). (For interpretation of the references to color in this figure legend, the reader is referred to the Web version of this article.)

2.4. Quantification of immuno-vascular indicators

Within each hexagon, $CD8^+$ cell and tissue-class areas were quantified. These hexagon-level $CD8^+$ cell counts were then converted to densities and, for each rank of the interface zone (−6 to +6), aggregated to rank-wise means and standard deviations for the tumor, stroma, and the TE (Fig. 1G). From these rank-wise profiles, two spatial indicators were computed: Immunodrop (ID) and Center of Mass (CM), which together describe the spatial dynamics of $CD8^+$ cell infiltration across the entire interface zone.

The ID (Equation (1)) represents the relative change in $CD8^+$ cell density across the TE and is calculated using the nearest close stromal and tumor ranks (−1 and + 1):

$$ID(q) = \frac{q(r_{-1})}{q(r_1)}$$

Equation (1). ID(q) – Immunodrop; $q(r)$ – $CD8^+$ cell density metric (mean or standard deviation) at rank r; $q(r_{-1})$ - $CD8^+$ cell density metric in the first stromal rank (−1); $q(r_1)$ - $CD8^+$ cell density metric in the first turmor rank (1).

The CM (Equation (2)) provides a broader assessment of immune cell location across the interface zone, identifying the center of immune cell mass along the rank axis. CM is calculated as follows:

$$CM(q) = \frac{\sum_{ri} r_i q(r_i)}{\sum_{ri} q(r_i)}$$

Equation (2). CM(q) – Center of Mass over rank-wise $CD8^+$ cell profiles; r_i – rank position in the tumor-stroma interface relative to the tumor edge ($r = 0$); $q(r_i)$ - a rank-wise summary of $CD8^+$ cell density metric at rank r_i across the interface zone.

A CM value closer to zero indicates a balanced immune distribution, whereas positive values suggest preferential immune localization toward the tumor, and negative values reflect stromal predominance. CM thus captures the spatial shift of immune cells in relation to the tumor.

For vascular analysis, the CD34-positive area was quantified within each hexagon and expressed as the vascular area fraction (VAF). VAF was computed within the peripheral intratumoral region (TE and tumor ranks +1 to +6). In addition to mean density and standard deviation of VAF, we also computed a VAF Center of Mass (VAF_CM) (Equation (3)).

$$VAF\_CM = \frac{\sum_{ri} r_i VAF(r_i)}{\sum_{ri} VAF(r_i)}$$

Equation (3). VAF_CM – Center of Mass of Vascular Area Fraction; r_i – rank position in the tumor interface relative to the tumor edge; $VAF(r_i)$ - mean Vascular area Fraction at rank r_i across the tumor edge.

VAF_CM indexes the position of the vascularity center along the rank axis: values closer to 0 indicate vascular concentration closer to TE, while higher positive values indicate a deeper, intratumorally centered vascular distribution.

2.5. Statistical analysis

Statistical analyses were performed using SAS software (version 9.4; SAS Institute Inc., Cary, NC, USA) and R (version 4.4.2; R Foundation for

Statistical Computing, Vienna, Austria) in the RStudio environment (RStudio, Inc., Boston, MA, USA). A two-tailed Welch's *t*-test was used to compare group means without assuming equal variances. Chi-squared and Fisher's exact tests were used to investigate the significant relationships among categorical clinicopathological factors. A nominal statistical significance threshold was established at $p < 0.05$.

Cutoff Finder [34] was used to determine the optimal cutoff value for each continuous variable in the full cohort for univariate evaluation of PFS. For variables dichotomized using these thresholds, PFS distributions were visualized using the Kaplan-Meier method and compared with the log-rank test. These derived thresholds were subsequently fixed and applied unchanged in all downstream survival and discrimination analyses.

Univariate Cox proportional hazards regression was used to assess associations of each candidate variable, including immunogradient, vessel markers and clinicopathological factors, with progression-free survival (PFS). Variables with $p < 0.05$ in univariate analysis were entered into multivariable Cox models to evaluate the independent prognostic value of immunogradient markers in relation to clinicopathological factors. Model building used stepwise likelihood-ratio testing. Results are reported as hazard ratios (HR) with 95% confidence intervals (CIs) and *p* values.

To derive prognostic models for PFS, variables retained as independent predictors in the final multivariable Cox regression models were combined into prognostic indices using two approaches. First, coefficient-based weighted indices were constructed using the regression coefficients from the corresponding multivariable Cox models. Predictors were coded in the adverse direction so that higher index values indicated higher risk; therefore, protective variables were recoded as their corresponding adverse categories. Second, simplified unweighted additive scores were generated by assigning 1 point to each independent adverse predictor included in the respective multivariable model. For the weighted indices, the coefficient assigned to each predictor was defined as follows:

$$\beta_i = \ln(HR_i)$$

Equation (4). β_i - regression coefficient for predictor *i*; HR_i – hazard ratio associated with predictor *i*; ln – natural logarithm.

Each patient's prognostic index was then computed as the sum of the corresponding β coefficients for present risk factors. For Kaplan-Meier visualization, the weighted indices were additionally categorized into low-, intermediate-, and high-risk groups according to tertiles.

Model discrimination for PFS was quantified with Harrell's C-index. 95% CIs were estimated using a nonparametric bootstrap with 1,000 resamples. Internal validation was performed with bootstrap optimism correction, refitting the model in each resample, evaluating performance on out-of-bag observations, estimating optimism, and subtracting it from the apparent C-index to obtain the optimism-corrected C-index. Predictor weights and cutoff values were derived in the full cohort and were not re-estimated within bootstrap resampling. Models were compared by absolute differences in optimism-corrected Harrell's C-index with corresponding 95% bootstrap confidence intervals.

3. Results

3.1. Univariate predictors of progression-free survival

In the univariate analysis, a number of clinicopathological variables were assessed to determine their impact on PFS. Variables that were under consideration can be broadly categorized into two main groups: clinicopathological data (routinely assessed in clinical practice) and the computed features, representing $CD8^+$ cell densities in different tissue compartments and their spatial shift (immunogradient) towards the tumor, together with CD34+-derived metrics of VAF within the peripheral intratumoral region. The analysis results are presented in Table 2.

Table 2
Univariate predictors of progression-free survival.

Variable	HR	95% CI	*p*-value
Demographic and clinical data			
Sex, female	0.37	0.18 – 0.79	0.007
Age (>54 years)	1.33	0.61 – 2.91	0.471
Multiple renal carcinomas	3.66	1.68 – 7.99	<0.001
Surgery type (partial nephrectomy vs. radical nephrectomy)	0.44	0.22 – 0.88	0.017
Kidney side (left vs. right)	0.75	0.40 – 1.43	0.384
Tumor size >4.95 cm	7.53	3.65 – 15.54	<0.001
Local recurrences	7.43	3.50 – 15.77	<0.001
Pathological data			
Grade (1-2 vs. 3-4)	3.42	1.70 – 6.90	<0.001
Coagulative tumor necrosis	6.93	3.53 – 13.60	<0.001
LVI status	2.74	1.38 – 5.45	0.003
pT stage (1 vs. 2, 3 or 4)	3.57	1.87 – 6.82	<0.001
R status	1.28	0.59 – 2.78	0.531
TME $CD8^+$ cell data			
Tumor_edge_CD8_m	3.61	1.70 – 7.64	<0.001
CD8_m_CM	2.24	0.99 – 5.10	0.047
Tumor_CD8_m	2.58	1.08 – 6.17	0.028
Stroma_CD8_m	2.43	1.11 – 5.30	0.021
Tumor_CD8_sd	3.76	1.65 – 8.56	<0.001
Stroma_CD8_sd	2.21	1.05 – 4.68	0.033
TME $CD34^+$ vascular data			
VAF_m_CM	0.28	0.12 – 0.64	0.001
Tumor_VAF_m	0.40	0.22 – 0.93	0.027
Tumor_VAF_sd	4.78	0.66 – 34.87	0.088

* HR – hazard ratio; CI – confidence interval; LVI – lymphovascular invasion; R – resection margin; CD8_m – $CD8^+$ cell density mean; m_CM – center of mass calculated from the means of $CD8^+$ cell density; CD8_sd – standard deviation of the $CD8^+$ cell density; CM_sd – center of mass calculated from the standard deviations of $CD8^+$ cell density; VAF_m_CM – center of mass calculated from the means of vascular area fraction in the tumor periphery; Tumor_VAF_m – mean vascular area fraction in the tumor periphery; Tumor_VAF_sd – standard deviation of vascular area fractions in the tumor periphery.

The univariate analysis revealed several clinical and pathological factors that correlated with worse PFS, including larger tumor size, multiple renal carcinomas (whether bilateral or unilateral), advanced pT stage, the presence of lymphovascular invasion and coagulative necrosis, and high tumor grade. By contrast, female sex was associated with longer PFS. Partial nephrectomy was associated with a lower hazard than radical nephrectomy in univariate analysis. This likely reflects confounding by indication, because nephron-sparing surgery is typically selected for smaller, less advanced tumors, rather than a causal benefit of the procedure itself.

Higher $CD8^+$ cell densities and greater dispersion in both tumor and stromal compartments (as reflected by the mean density and standard deviation metrics), as well as higher mean density at the TE, were all associated with worse prognosis. For CD34-derived vascular metrics, greater intratumoral vascular coverage and deeper centering of the

vascular area within the tumor tissue were associated with longer PFS. In contrast, higher dispersion of vascular area within the tumor trended toward worse PFS but did not reach statistical significance. These observations underscore the potential prognostic value of analyzing spatial patterns of $CD8^+$ infiltration and intratumoral $CD34^+$ vascularization. The Kaplan-Meier survival plots for each significant variable that also represented independent prognostic features by multivariable Cox regression (see below) are presented in Fig. 3.

3.2. Independent predictors of progression-free survival

Independent prognostic features on PFS in ccRCC patients were assessed using multivariable Cox regression models. The analysis was first performed using standard demographic and clinical data, then supplemented with pathological data, $CD8^+$ cell densities, and gradient indicators from the tumor-stroma interface, as well as CD34+-derived vascular metrics of VAF from the tumor periphery, and follow-up variables (Table 3).

In Model 1, based on demographic and clinical data only (LR: 48.63, $p < 0.0001$), male sex, multiple renal carcinomas, and tumor size >4.95 cm were independently associated with shorter PFS. After addition of pathological variables in Model 2 (LR: 65.13, $p < 0.0001$), coagulative tumor necrosis emerged as an additional independent adverse prognostic factor, while male sex, multiple renal carcinomas, and tumor size remained significant. In Model 3, which integrated spatial immunohistochemical variables and served as the Baseline model (LR: 68.01, $p < 0.0001$), male sex, tumor size >4.95 cm, coagulative tumor necrosis, and CD8_m_CM remained independently associated with shorter PFS. Specifically, a spatial shift of $CD8^+$ cell density toward the tumor side of the interface was associated with worse outcome (HR: 3.24, 95% CI: 1.62-6.49, $p = 0.001$), indicating that spatial immune organization provides prognostic information beyond standard clinicopathological factors. Model 4 additionally incorporated local recurrence during follow-up and was therefore considered a Disease-Course model rather than a baseline decision tool (LR: 93.01, $p < 0.0001$). In this model, local recurrence was the strongest adverse predictor of shorter PFS (HR: 17.69, 95% CI: 7.17-43.68, $p < 0.001$), while male sex, tumor size >4.95 cm, coagulative tumor necrosis, and CD8_m_CM remained

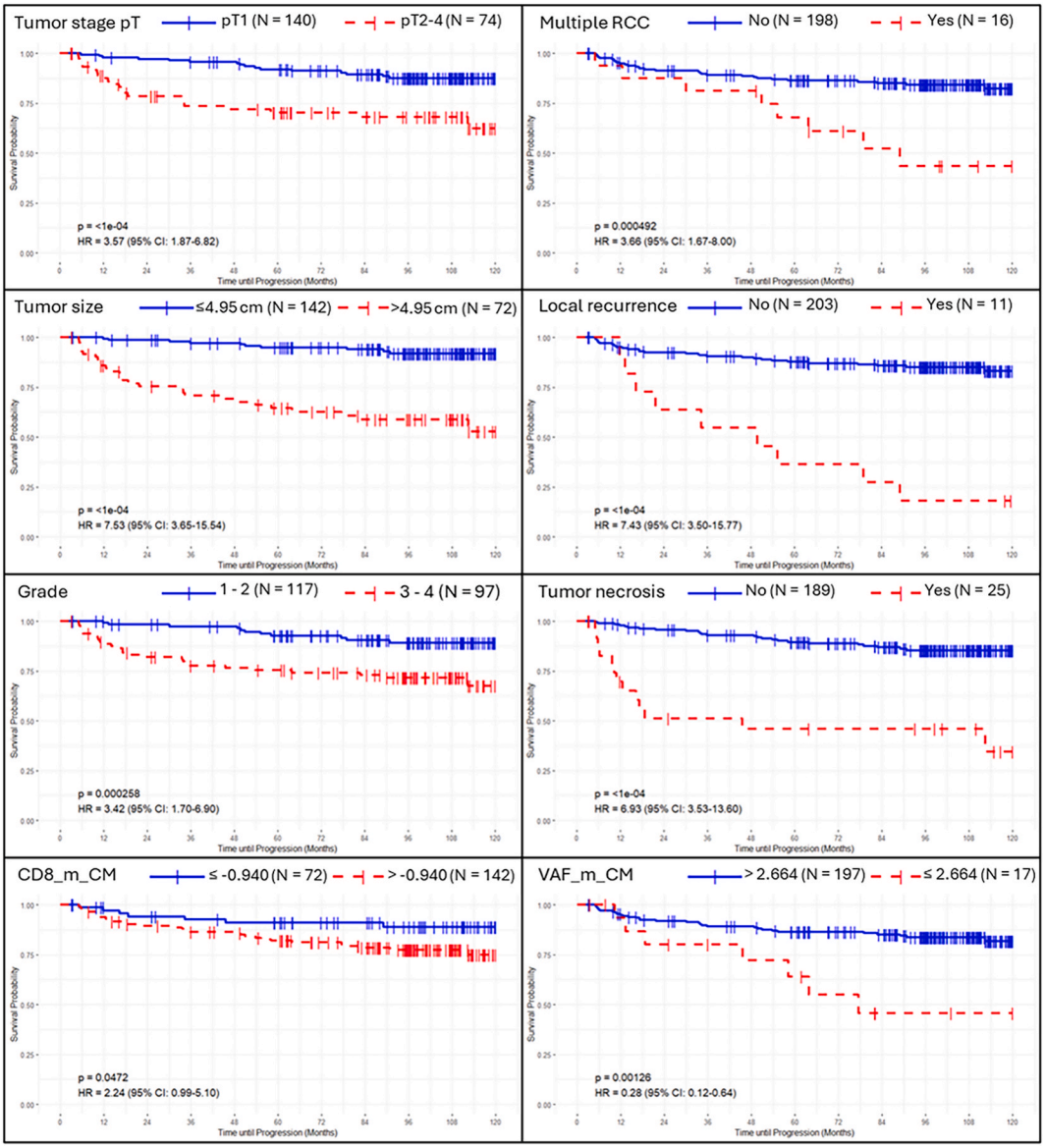

Fig. 3. Kaplan-Meier Progression-free survival (PFS) plots for clinicopathological and immunogradient prognostic factors identified by univariate Cox regression analysis: (a) Tumor stage; (b) Multiple renal carcinomas; (c) Tumor size; (d) Local recurrence; (e) Grade; (f) Presence of tumor necrosis; (g) Center of mass of the $CD8^+$ cell means; (h) Center of mass of the vascular area fraction means.

Table 3
Independent predictors of PFS in ccRCC patients based on multivariable Cox regression.

PFS Model 1: demographic and clinical data				
LR: 48.63, $p < 0.0001$, N = 214				
Variable	HR	95% CI	*p*-value	χ2
Sex (female vs male)	0.40	0.19 – 0.84	0.016	5.84
Multiple renal carcinomas	3.06	1.40 – 6.69	0.005	7.86
Tumor size >4.95 cm	7.38	3.58 – 15.21	<0.001	29.31
PFS Model 2: demographic, clinical, and pathological data				
LR: 65.13, $p < 0.0001$, N = 214				
Variable	HR	95% CI	*p*-value	χ2
Sex (female vs male)	0.37	0.18 – 0.80	0.011	6.52
Multiple renal carcinomas	3.38	1.54 – 7.43	0.003	9.16
Tumor size >4.95 cm	5.87	2.79 – 12.34	<0.001	21.75
Coagulative tumor necrosis	5.08	2.48 – 10.38	<.0001	19.85
PFS Model 3: demographic, clinical, pathological, and spatial IHC data				
LR: 68.01, $p < 0.0001$, N = 214				
Variable	HR	95% CI	*p*-value	χ2
Sex (female vs male)	0.29	0.14 – 0.63	0.002	9.99
Tumor size >4.95 cm	6.30	2.97 – 13.40	<0.001	22.90
Coagulative tumor necrosis	6.03	2.86 – 12.71	<0.001	22.30
CD8_m_CM	3.24	1.62 – 6.49	0.001	11.00
PFS Model 4: demographic, clinical, pathological, spatial IHC, and local recurrence data				
LR: 93.01, $p < 0.0001$, N = 214				
Variable	HR	95% CI	*p*-value	χ2
Sex (female vs male)	0.45	0.21 – 0.99	0.047	3.94
Tumor size >4.95 cm	7.14	3.27 – 15.60	<0.001	24.27
Coagulative tumor necrosis	5.14	2.66 – 12.54	<0.001	19.71
Local recurrence during follow-up	17.69	7.17 – 43.68	<0.001	38.84
CD8_m_CM	5.14	1.96 – 13.46	0.001	11.10
VAF_ m_CM	0.32	0.13 – 0.80	0.014	6.02

* PFS – progression-free survival; HR – hazard ratio; CI – confidence interval; LR – likelihood ratio; CD8_m_CM – center of mass calculated from the mean $CD8^+$ cell density; VAF_m_CM – center of mass calculated from the mean of vascular area fraction in the tumor periphery.

independently significant. In addition, VAF_m_CM was independently associated with longer PFS (HR: 0.32, 95% CI: 0.13-0.80, p = 0.014), indicating that a more tumor-centered vascular area distribution in the peripheral tumor region provides complementary prognostic information during disease course assessment.

3.3. Coefficient-based prognostic indices for PFS

Based on the independent predictors retained in the final multivariable Cox regression models, coefficient-based weighted prognostic indices for PFS were constructed using the exact regression coefficients, thereby preserving the relative prognostic contribution of each variable. Finally, two prognostic formulations were developed: a Baseline prognostic index (Model 3), based exclusively on variables available at baseline, and a Disease-Course prognostic index (Model 4), which additionally incorporated local recurrence during follow-up and the vascular spatial marker of low VAF_m_CM.

- **Baseline prognostic index** = 1.238 × (male sex) + 1.841 × (tumor size>4.95 cm) + 1.797 × (coagulative necrosis) + 1.176 × (high CD8_m_CM).
- **Disease-Course prognostic index** = 0.799 × (male sex) + 1.966 × (tumor size>4.95 cm) + 1.637 × (coagulative necrosis) + 2.873 × (local recurrence) + 1.637 × (high CD8_m_CM) + 1.139 × (low VAF_m_CM).

To facilitate clinical interpretability, the continuous prognostic indices were further used to stratify patients into three risk groups based on tertile-derived cutoffs. For the Baseline prognostic index, the low-, intermediate-, and high-risk groups were defined by index values of ≤1.2380, >1.2380 to ≤2.9730, and >2.9730, respectively. For the Disease-Course prognostic index, the corresponding groups were defined as ≤ 1.637, >1.637 to ≤2.873, and >2.873, respectively. Kaplan-Meier analysis showed significant differences in PFS among the tertile-defined risk groups for both the Baseline prognostic index and the Disease-Course prognostic index (overall log-rank p < 0.001 for both) (Fig. 4A and B).

As a simplified exploratory comparison, we also derived unweighted additive prognostic scores for both multivariable models by assigning 1 point to each independent adverse prognostic factor. For the Baseline Model, the adverse factors were male sex, tumor size >4.95 cm, coagulative tumor necrosis, and high CD8_m_CM. Patients were stratified into three risk groups according to the total score: low-risk (0 to 1 point), intermediate-risk (2 points), and high-risk (3 to 4 points). For the Disease-Course Model, the adverse factors were male sex, tumor size >4.95 cm, coagulative tumor necrosis, local recurrence during follow-up, high CD8_m_CM, and low VAF_m_CM. Patients were similarly stratified into low-risk (0 to 1 point), intermediate-risk (2 points), and high-risk (3 to 6 points) groups. Kaplan-Meier analysis showed significant differences in PFS across the risk groups for both unweighted additive scores (log-rank p < 0.0001) (Fig. 4C and D).

3.4. Discrimination and comparison with established scoring systems

Discriminative performance for PFS was assessed using Harrell's C-index with bootstrap-derived 95% confidence intervals, and optimism-corrected estimates were calculated to account for potential overfitting. Among the internally developed models, the coefficient-based weighted Disease-Course Model showed the highest apparent discrimination, with a C-index of 0.889 (95% CI: 0.84 to 0.94), followed by the unweighted Disease-Course Model at 0.861 (95% CI: 0.81 to 0.91). For baseline prediction, the coefficient-based weighted Baseline Model achieved a slightly higher apparent C-index than the unweighted Baseline Model, reaching 0.820 (95% CI: 0.75 to 0.89) versus 0.810 (95% CI: 0.74 to 0.87).

Among established clinicopathological scoring systems, the SSIGN score yielded an apparent C-index of 0.759 (95% CI: 0.67 to 0.83), whereas the GRANT score showed substantially lower discrimination at 0.579 (95% CI: 0.50 to 0.66) (Fig. 5). Overall, both internally developed models outperformed the established scoring systems. Coefficient-based weighting provided a modest gain in discrimination for the Baseline Model and a more pronounced improvement for the Disease-Course Model.

The optimism-corrected C-indices were very similar to the apparent estimates, reaching 0.819 for the weighted Baseline Model, 0.888 for the weighted Disease-Course Model. These findings indicate that the predictive performance of the developed models remained stable after internal validation, with the weighted Disease-Course Model showing the best overall prognostic discrimination for PFS.

4. Discussion

Our study reveals that spatial patterns of immune cell and microvasculature density distributions in nephrectomy samples from ccRCC patients can predict PFS. Specifically, the directional shift of these densities across the tumor-stroma interface, quantified as their CM, provides independent prognostic value. While the shift of $CD8^+$ cells toward the tumor compartment predicted shorter PFS, the relative increase of the microvascular area toward the tumor compartment was associated with longer PFS. Furthermore, these indicators maintained their independent impact in the prognostic models derived from standard clinical and pathology features.

$CD8^+$ cells are the most powerful effectors in the anti-tumor immune response and constitute the backbone of immunotherapy [35]. Across various malignancies (colorectal, breast, ovarian, bladder, and others),

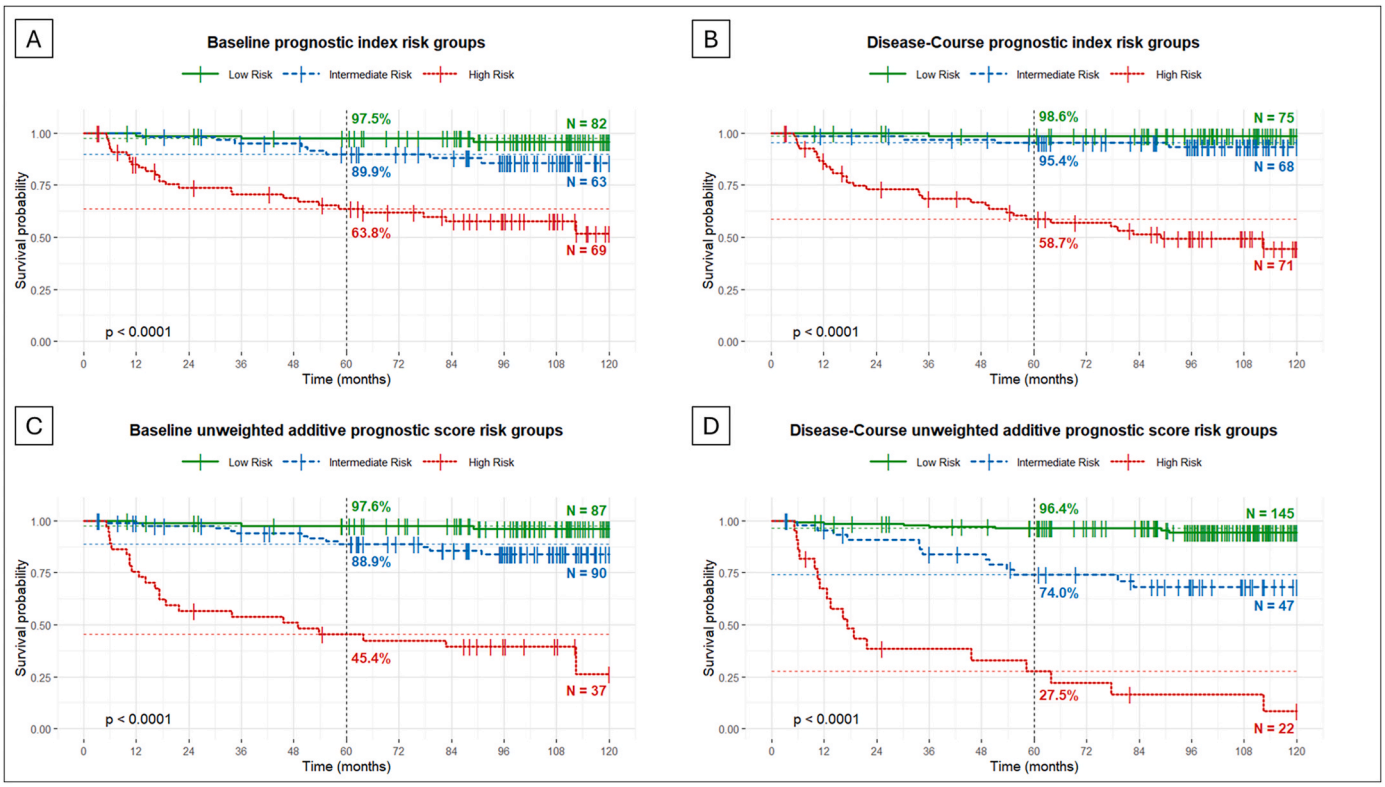

Fig. 4. Kaplan-Meier curves for progression-free survival by coefficient-based prognostic index and unweighted additive prognostic score: (a) Baseline prognostic index risk groups from the weighted Baseline Model (Model 3), based on male sex, tumor size >4.95 cm, coagulative tumor necrosis, and high CD8_m_CM; (b) Disease-Course prognostic index risk groups from the weighted Disease-Course Model (Model 4), based on male sex, tumor size >4.95 cm, coagulative tumor necrosis, local recurrence during follow-up, high CD8_m_CM, and low VAF_m_CM; (c) Baseline unweighted additive prognostic score risk groups based on the same four adverse predictors, with 1 point assigned to each factor; (d) Disease-Course unweighted additive prognostic score risk groups based on the same six adverse predictors, with 1 point assigned to each factor.

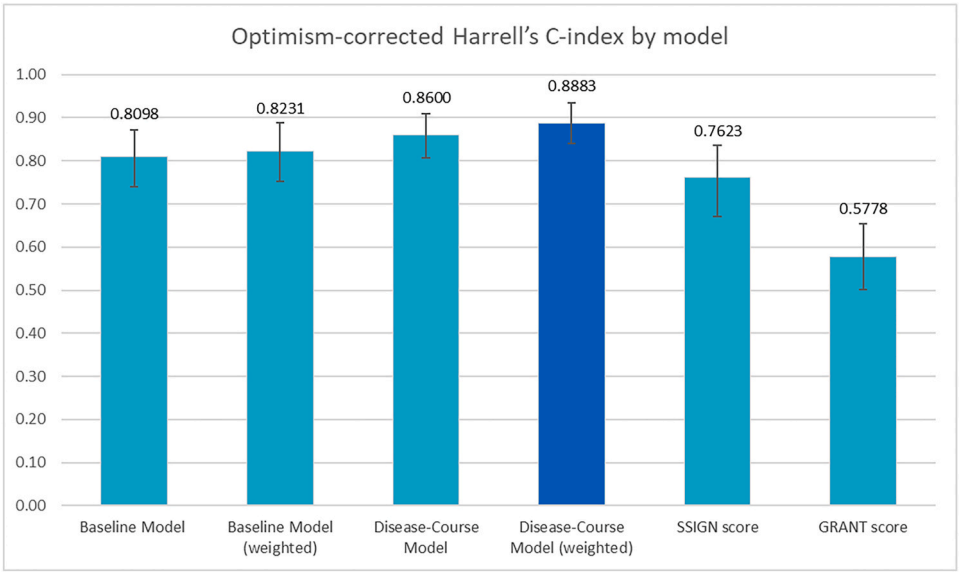

Fig. 5. Bootstrap optimism-corrected Harrell's C-indices of the prognostic indices for progression-free survival: Baseline additive prognostic index, Baseline weighted prognostic index, Disease-Course additive prognostic index, Disease-Course weighted prognostic index, SSIGN score (stage, size, grade, and necrosis), and GRANT score (Grade, Age, Nodes, and Tumor).

their prevalence reliably predicts response to anti-PD-1/PD-L1 therapy [36]. However, the prognostic significance of $CD8^+$ cell infiltration in ccRCC remains controversial. Similar to our findings, several studies [14,17] have reported that, unlike in many other solid tumors, a high density of $CD8^+$ cell infiltration in ccRCC often correlates with worse clinical outcomes. This phenomenon likely arises from an immunosuppressive microenvironment of ccRCC, where chronic antigen exposure and strong immune checkpoint signaling lead to dysfunctional or

"exhausted" $CD8^+$ cells characterized by elevated expression of PD-1, CTLA-4, and other markers [14,17,37,38]. Indeed, the pro-inflammatory or angiogenic milieu of ccRCC fosters tumor progression, rendering the mere presence of $CD8^+$ cells insufficient to mount an effective anti-tumor response and instead signaling immunological "dysfunction" [18,19]. Our findings reinforce this paradox: a higher CM, reflecting a shift of $CD8^+$ cell densities toward the tumor side of the interface, remained independently associated with shorter PFS both in the Baseline model (HR 3.24; p = 0.001) and in the Disease-Course model that additionally accounted for local recurrence during follow-up (HR 5.14; p = 0.001). These observations highlight the importance of evaluating not only immune cell presence, but also their spatial organization in ccRCC, emphasizing mechanisms of T-cell dysfunction and exhaustion that distinguish this disease from the more favorable $CD8^+$ profiles observed in other solid tumors.

Unlike simple measures of immune cell densities, our analysis of CM provides insight into spatial immune distribution across the tumor-stroma interface and may function as a computational biomarker of the anti-tumor immune response. While conventional frameworks often categorize the TME into rigid "hot," "cold," or "excluded" phenotypes [39,40], the CD8 CM indicator offers a more nuanced, continuous measure of spatial distribution. The CM summarizes where CD8 cell density signal is centered along the stroma-to-tumor axis, which more closely reflects an excluded-like to tumor-shifted continuum than a simple hot-versus-cold distinction. Importantly, high CM does not necessarily indicate a globally "hot" tumor, because it may also occur when the overall CD8 burden is low but relatively shifted toward the tumor aspect of the interface. These findings suggest that immune phenotypes in ccRCC may not be fully captured by discrete categories alone and may be better represented as continuous spatial features.

Similar core-and-margin frameworks, including the Immunoscore in colorectal cancer initially proposed by Galon et al. [41], have demonstrated robust prognostic value and have been examined across other malignancies [23,42–45]. Related core and margin approaches have shown prognostic value in bladder cancer, where higher $CD8^+$ density at the invasive margin and a higher Immunoscore correlated with improved DFS and OS after cystectomy [46]. Building on Immunoscore concepts, studies in ccRCC reveal that spatially-resolved indicators outperform simple immune-cell counts or densities. Using imaging mass cytometry, Zhang et al. [47] identified four reproducible immune architectures in ccRCC in which TLS-like and granzyme B-positive $CD8^+$ with B-cell neighborhoods were associated with favorable outcomes, whereas macrophage- or Treg-enriched neighborhoods were linked to worse survival. Consistently, Chakiryan et al. [48] using multiplex immunofluorescence with geospatial statistics, showed that spatial patterns at the tumor-stroma interface provide independent prognostic information; for example, clustering of CD163-positive M2-like tumor-associated macrophages in the stroma and $CD8^+$ with CD163+ colocalization predicted worse OS and cancer-specific survival, tracked with poorer systemic therapy responses, and coincided with terminal T-cell exhaustion [48]. Concordant evidence indicates that the distribution of $CD8^+$ and FoxP3+ T-cells, or the presence of $CD39^+$ $CD8^+$ "dysfunctional" T-cells, refines prognostic assessment beyond standard clinicopathological features [19,49–51]. Our findings support integrating spatial immune metrics into routine prognostic scoring in ccRCC and provide evidence for the performance of the interface-zone immunogradient indicator previously tested in other solid tumors [21,52].

Angiogenesis constitutes another disease-defining axis in ccRCC. Induced by VHL loss, HIF stabilization, and VEGF-driven neovascularization [25], we tested whether the spatial pattern of relative microvasculature topology at the tumor periphery carries prognostic value. We found that higher VAF_CM, representing a centripetal positioning of $CD34^+$ vascular area within tumor peripheral ranks of the interface, was associated with longer PFS. Although VAF_CM was not retained as an independent predictor in the Baseline model, it remained independently protective in the multivariable Disease-Course model (HR 0.32; $p = 0.014$), while the adverse effect of $CD8^+$ cell gradient toward the tumor persisted (HR 5.14; $p = 0.0001$). By quantifying VAF within the peripheral intratumoral region and modeling its CM, our approach captures organizational properties of angiogenesis that are not reflected by absolute counts. This topography-specific effect suggests that more centrally abundant microvasculature may mitigate hypoxia, reduce chaotic angiogenesis, and restrain aggressive behavior, in contrast to $CD8^+$ cell shifts toward the tumor, which likely reflect dysfunctional and exhausted cells resulting in an immunosuppressive milieu.

Across studies analyzing microvasculature in ccRCC, conventional pan-endothelial MVD has shown limited and often contradictory prognostic impact. Two meta-analyses synthesizing 1997 – 2014 studies reported no significant association between higher MVD and OS. The prognostic effect varied by marker and quantification approach, underscoring that undifferentiated counting conflates vessel maturity and ignores spatial context [30,53]. In contrast, studies that refine what is measured or where it is measured do retrieve prognostic information. Automated whole-slide analysis normalizing tumor $CD34^+$ counts to the adjacent renal medulla found that a higher adjusted MVD (tumor/-normal ratio) was independently associated with shorter DFS, whereas unadjusted MVD was non-informative [54], suggesting that global hypervascularization marks aggressive biology and the way vascularity is referenced substantially changes its prognostic value. More recent frameworks, such as the IMmotion study, move beyond simple counts, showing that histologic vascular patterning correlates with outcome and links to myeloid-rich immune states, while transcriptomic angiogenesis signatures predict VEGF-targeted therapy benefit [55]. Likewise, Kaneko et al. found that three-dimensional light-sheet phenotyping links volumetric CD34 and LYVE-1 features, including vessel radius and density distributions, to survival, and that blood vessel radius differed in tumors with PI3K–mTOR pathway mutations, underscoring the importance of vascular geometry [56]. Our data support these results, confirming that absolute vessel counts lack prognostic value and underestimate the importance of vessel topology. A higher VAF_CM was protective for PFS, consistent with centripetal enrichment that presumably stabilizes oxygenation and restrains hypoxia-driven aggression. Conversely, vascular networks spatially skewed toward the tumor border or disorganized networks likely capture the adverse, immature angiogenic state as implied by our findings.

Although T cells extravasate through blood vessels, a direct spatial correlation between CD8 and CD34 signals is not necessarily expected. This was supported by our data: the CD8 and CD34 CM metrics did not reveal significant association in our cohort (Spearman's rho = 0.113, p = 0.101), suggesting that these biomarkers reflect partly distinct dimensions of the ccRCC microenvironment rather than a single linear immune-vascular process. CD34 immunostaining quantifies endothelial-lined vascular area, but it does not report vessel functionality, endothelial activation, or immune-permissive adhesion pathways required for leukocyte trafficking [57,58]. Tumor endothelium can exhibit "endothelial anergy" under angiogenic signaling. This reduced expression of key adhesion molecules such as ICAM-1, VCAM-1, and selectins, limits immune cell extravasation despite the presence of vascular structures [59]. Consistent with this, reviews of immune–vascular crosstalk show that vascular normalization, rather than vessel quantity alone, is linked to improved perfusion and enhanced immune effector infiltration [32,60]. In ccRCC specifically, several studies report that intratumoral CD8 infiltration or particular CD8 cell subsets can associate with poor outcomes, reflecting dysfunctional or exhausted states [61,62]. Therefore, the opposite prognostic directions of our CD8 localization metric and CD34-derived vascular topology metric likely indicate that these biomarkers may capture complementary but partly decoupled dimensions of the ccRCC microenvironment rather than a single linear process.

Our study identified several key predictors of worse PFS in ccRCC. Notably, coagulative tumor necrosis emerged as a strong indicator of

aggressive disease. Originally described as a marker of poor RCC behavior in the 1970s, it is typically associated with larger tumor size, higher grade, and increased proliferative activity [63,64]. In our study, tumor size greater than 4.95 cm was another robust predictor of worse PFS, echoing multiple prognostic models, such as the Mayo Clinic SSIGN score, where increasing size thresholds portend progressively worse outcomes [65]. Female sex was also independently associated with longer PFS, consistent with reports that men more often present with more aggressive RCC and may exhibit less effective antitumor immunity, potentially influenced by androgen receptor signaling [66,67]. Local recurrence, noted in 5.14% of our cohort, was the most significant predictor of worse PFS in the Disease-Course Model (HR 17.69; $p < 0.0001$), with most of these patients subsequently developing metastases. Although local recurrence often confers a high mortality risk [68–70], timely surgical intervention can yield encouraging three-year cancer-specific survival rates, particularly if combined with systemic therapy. Consequently, vigilant surveillance and prompt, aggressive treatment strategies are vital for patients at high risk or those presenting with local recurrences [71].

From a clinical perspective, our findings are best interpreted through two complementary prognostic frameworks. The Baseline model, which includes only variables available at the time of nephrectomy, is more suitable for immediate postoperative risk stratification and better reflects current adjuvant decision pathways, in which consideration of systemic therapy such as pembrolizumab is based on baseline pathological risk rather than events arising later during follow-up [65,72]. In contrast, the Disease-Course model, which incorporates local recurrence, is not intended as a baseline treatment-selection tool but rather as a dynamic postoperative risk-refinement model. This distinction is clinically relevant because complete resection remains the preferred potentially curative option for isolated local recurrence when feasible, whereas the role and timing of additional systemic therapy beyond surgery remain less clearly defined [65]. In this setting, combining recurrence status with spatial tumor microenvironment markers may help distinguish patients suitable for local treatment and surveillance from those who may warrant earlier treatment escalation. Importantly, in a sensitivity analysis restricted to patients without local recurrence, CD8 CM remained an independent predictor of shorter PFS (HR 6.44, 95% CI 1.53 to 27.20, $p = 0.011$), supporting that its prognostic value is not merely a surrogate for recurrence.

Our study has some limitations. First, it was conducted retrospectively at a single center, which may limit generalizability. Minor inconsistencies in the tissue classifier occasionally led to misclassified foci, which we mitigated by applying a 1000 μm^2 minimum object size filter. We also examined only one representative FFPE block per patient, potentially underrepresenting the spatial macro-level heterogeneity of the TME. For vascular analysis, we confined CD34 quantification to the periphery of the tumor compartment and measured vessel area rather than counts, which may miss vessel maturity. Finally, CD8 and CD34 were stained on separate, consecutive tissue sections, so exact cell-vessel colocalization could not be assessed. Further studies that validate our findings with larger cohorts, multiplex staining, and additional markers of vessel maturity, hypoxia, and immune cell exhaustion/checkpoints are needed.

5. Conclusions

We propose spatially-resolved computational biomarkers reflecting the tissue immune response and microvasculature organization at the tumor-stroma interface in ccRCC. In post-nephrectomy patients, at baseline, a tumor-shifted $CD8^+$ spatial profile provided independent prognostic information beyond standard clinicopathological factors, while CD34-derived vascular topology contributed complementary prognostic value during disease-course assessment. These findings suggest that spatial immune-vascular profiling may refine current postoperative risk stratification in ccRCC.

CRediT authorship contribution statement

Mantas Fabijonavicius: Writing – original draft, Visualization, Methodology, Investigation, Formal analysis, Data curation, Conceptualization. **Ausra Garnelyte:** Writing – review & editing, Methodology, Investigation, Formal analysis. **Dovile Zilenaite-Petrulaitiene:** Writing – review & editing, Software, Methodology, Formal analysis, Data curation. **Allan Rasmusson:** Writing – review & editing, Visualization, Software, Methodology. **Julius Drachneris:** Writing – review & editing, Methodology, Investigation, Formal analysis. **Albertas Cekauskas:** Writing – review & editing, Conceptualization. **Feliksas Jankevicius:** Writing – review & editing, Resources, Conceptualization. **Arvydas Laurinavicius:** Writing – review & editing, Visualization, Supervision, Resources, Project administration, Methodology, Investigation, Conceptualization.

Informed consent statement

Patient consent was waived by the Lithuanian Bioethics Committee according to the International Ethical Guidelines for Health-related Research Involving Humans [73].

Institutional review board statement

This study was conducted in accordance with the Declaration of Helsinki and approved by the Vilnius Regional Biomedical Research Ethics Committee (research permit No. 2024/9-1600-1062 issued on September 2024).

Data availability statement

The datasets generated and analyzed during the current study are available in the Zenodo repository, [https://doi.org/10.5281/zenodo.17603823]. Raw whole-slide images contain potentially identifiable information and are not publicly shareable due to institutional and ethical restrictions; de-identified derived features are available in the repository as described.

Funding

No external funding was received.

Declaration of competing interest

The authors declare no conflicts of interest. The funders had no role in study design, data collection and analysis, decision to publish, or preparation of the manuscript.

Acknowledgements

Research was conducted as part of the execution of Project ”Mission-driven Implementation of Science and Innovation Programmes“ (No. 02-002-P-0001), funded by the Economic Revitalization and Resilience Enhancement Plan ”New Generation Lithuania”.

List of abbreviations:

$CD8^+$ – cytotoxic T lymphocyte marker
ccRCC – clear cell renal cell carcinoma
RCC – renal cell carcinoma
PFS – progression-free survival
TNM – tumor-node-metastasis
UISS – UCLA Integrated Staging System
MSKCC – Memorial Sloan-Kettering Cancer Center
SSIGN – Stage, Size, Grade, and Necrosis
TME – tumor microenvironment

ICI – immune checkpoint inhibitor
VHL – von Hippel-Lindau
HIF – hypoxia-inducible factor
VEGF – vascular endothelial growth factor
mTOR – mechanistic target of rapamycin
MVD – microvessel density
VWF – von Willebrand factor
MVA – microvessel area
H&E – hematoxylin and eosin
FFPE – formalin-fixed paraffin-embedded
IHC – immunohistochemistry
AI – artificial intelligence
DIA – digital image analysis
TE – tumor edge
ID – Immunodrop
CM – center of mass
HR – hazard ratio
CI – confidence interval
LVI – lymphovascular invasion
ISUP/WHO – International Society of Urologic Pathologists/World Health Organization
LR – log-rank test
CD8_m_CM – center of mass calculated from the mean $CD8^+$ cell density
$CD34^+$ – endothelial marker for microvessels
VAF – vascular area fraction
VAF_CM – center of mass of the mean VAF in the tumor periphery
PD-1 – programmed cell death protein 1
PD-L1 – programmed death-ligand 1
CTLA-4 – cytotoxic T-lymphocyte-associated protein 4
DFS – disease-free survival
CSS – cancer-specific survival
LYVE-1 – lymphatic vessel endothelial hyaluronan receptor 1
Tumor_edge_CD8_m – mean $CD8^+$ cell density at the tumor edge
Tumor_CD8_m – mean $CD8^+$ cell density in tumor
Stroma_CD8_m – mean $CD8^+$ cell density in stroma
CD8_sd_CM – center of mass calculated from the standard deviation of $CD8^+$ density
Tumor_CD8_sd – standard deviation of $CD8^+$ density in tumor
Stroma_CD8_sd – standard deviation of $CD8^+$ density in stroma

References

[1] Bukavina L, Bensalah K, Bray F, et al. Epidemiology of renal cell carcinoma: 2022 update. Eur Urol 2022;82:529–42. https://doi.org/10.1016/j.eururo.2022.08.019.
[2] Jonasch E, Walker CL, Rathmell WK. Clear cell renal cell carcinoma ontogeny and mechanisms of lethality. Nat Rev Nephrol 2021;17:245–61. https://doi.org/10.1038/s41581-020-00359-2.
[3] Zisman A, Pantuck AJ, Wieder J, et al. Risk group assessment and clinical outcome algorithm to predict the natural history of patients with surgically resected renal cell carcinoma. J Clin Oncol Off J Am Soc Clin Oncol 2002;20:4559–66. https://doi.org/10.1200/JCO.2002.05.111.
[4] Kattan MW, Reuter V, Motzer RJ, et al. A postoperative prognostic nomogram for renal cell carcinoma. J Urol 2001;166:63–7. https://doi.org/10.1016/S0022-5347(05)66077-6.
[5] Frank I, Blute ML, Cheville JC, et al. An outcome prediction model for patients with clear cell renal cell carcinoma treated with radical nephrectomy based on tumor stage, size, grade and necrosis: the SSIGN score. J Urol 2002;168:2395–400. https://doi.org/10.1016/S0022-5347(05)64153-5.
[6] Ferro M, Musi G, Marchioni M, et al. Radiogenomics in renal cancer management—current evidence and future prospects. Int J Mol Sci 2023;24:4615. https://doi.org/10.3390/ijms24054615.
[7] Schuettfort VM, Pradere B, Rink M, et al. Pathomics in urology. Curr Opin Urol 2020;30:823. https://doi.org/10.1097/MOU.0000000000000813.
[8] Correa AF, Jegede O, Haas NB, et al. Predicting renal cancer recurrence: defining limitations of existing prognostic models with prospective trial-based validation. J Clin Oncol Off J Am Soc Clin Oncol 2019;37:2062–71. https://doi.org/10.1200/JCO.19.00107.
[9] Quail DF, Joyce JA. Microenvironmental regulation of tumor progression and metastasis. Nat Med 2013;19:1423–37. https://doi.org/10.1038/nm.3394.
[10] Hinshaw DC, Shevde LA. The tumor microenvironment innately modulates cancer progression. Cancer Res 2019;79:4557–66. https://doi.org/10.1158/0008-5472.CAN-18-3962.
[11] Joyce JA, Pollard JW. Microenvironmental regulation of metastasis. Nat Rev Cancer 2009;9:239–52. https://doi.org/10.1038/nrc2618.
[12] Vuong L, Kotecha RR, Voss MH, et al. Tumor microenvironment dynamics in clear cell renal cell carcinoma. Cancer Discov 2019;9:1349–57. https://doi.org/10.1158/2159-8290.CD-19-0499.
[13] Gentles AJ, Newman AM, Liu CL, et al. The prognostic landscape of genes and infiltrating immune cells across human cancers. Nat Med 2015;21:938–45. https://doi.org/10.1038/nm.3909.
[14] Fridman WH, Zitvogel L, Sautès–Fridman C, et al. The immune contexture in cancer prognosis and treatment. Nat Rev Clin Oncol 2017;14:717–34. https://doi.org/10.1038/nrclinonc.2017.101.
[15] Nearchou IP, Lillard K, Gavriel CG, et al. Automated analysis of lymphocytic infiltration, tumor budding, and their spatial relationship improves prognostic accuracy in colorectal cancer. Cancer Immunol Res 2019;7:609–20. https://doi.org/10.1158/2326-6066.CIR-18-0377.
[16] Nakano O, Sato M, Naito Y, et al. Proliferative activity of intratumoral CD8(+) T-lymphocytes as a prognostic factor in human renal cell carcinoma: clinicopathologic demonstration of antitumor immunity. Cancer Res 2001;61:5132–6.
[17] Giraldo NA, Becht E, Vano Y, et al. Tumor-infiltrating and peripheral blood T-cell immunophenotypes predict early relapse in localized clear cell renal cell carcinoma. Clin Cancer Res 2017;23:4416–28. https://doi.org/10.1158/1078-0432.CCR-16-2848.
[18] Granier C, Dariane C, Combe P, et al. Tim-3 expression on tumor-infiltrating PD-1+ CD8+ T cells correlates with poor clinical outcome in renal cell carcinoma. Cancer Res 2017;77:1075–82. https://doi.org/10.1158/0008-5472.CAN-16-0274.
[19] Qi Y, Xia Y, Lin Z, et al. Tumor-infiltrating CD39+CD8+ T cells determine poor prognosis and immune evasion in clear cell renal cell carcinoma patients. Cancer Immunol Immunother 2020;69:1565–76. https://doi.org/10.1007/s00262-020-02563-2.
[20] Speiser DE, Ho P-C, Verdeil G. Regulatory circuits of T cell function in cancer. Nat Rev Immunol 2016;16:599–611. https://doi.org/10.1038/nri.2016.80.
[21] Rasmusson A, Zilenaite D, Nestarenkaite A, et al. Immunogradient indicators for antitumor response assessment by automated tumor-stroma interface zone detection. Am J Pathol 2020;190:1309–22. https://doi.org/10.1016/j.ajpath.2020.01.018.
[22] Selvi I, Demirci U, Bozdogan N, et al. The prognostic effect of immunoscore in patients with clear cell renal cell carcinoma: preliminary results. Int Urol Nephrol 2019;52:21–34. https://doi.org/10.1007/s11255-019-02285-0.
[23] Kirilovsky A, Marliot F, El Sissy C, et al. Rational bases for the use of the immunoscore in routine clinical settings as a prognostic and predictive biomarker in cancer patients. Int Immunol 2016;28:373–82. https://doi.org/10.1093/intimm/dxw021.
[24] Guo C, Zhao H, Wang Y, et al. Prognostic value of the neo-immunoscore in renal cell carcinoma. Front Oncol 2019;9:439. https://doi.org/10.3389/fonc.2019.00439.
[25] Ohe C, Yoshida T, Amin MB, et al. Development and validation of a vascularity-based architectural classification for clear cell renal cell carcinoma: correlation with conventional pathological prognostic factors, gene expression patterns, and clinical outcomes. Mod Pathol 2022;35:816–24. https://doi.org/10.1038/s41379-021-00982-9.
[26] Jilaveanu LB, Puligandla M, Weiss SA, et al. Tumor microvessel density as a prognostic marker in high-risk renal cell carcinoma patients treated on ECOG-ACRIN E2805. Clin Cancer Res 2018;24:217–23. https://doi.org/10.1158/1078-0432.CCR-17-1555.
[27] Han E, Kim J, Jung MJ, et al. ERG and nestin: useful markers of immature vessels and novel prognostic markers in renal cell carcinoma. Int J Clin Exp Pathol 2021;14:116–25.
[28] Sato M, Nakai Y, Nakata W, et al. Microvessel area of immature vessels is a prognostic factor in renal cell carcinoma. Int J Urol Off J Jpn Urol Assoc 2014;21:130–4. https://doi.org/10.1111/iju.12231.
[29] Baldewijns MM, Thijssen VL, Van den Eynden GG, et al. High-grade clear cell renal cell carcinoma has a higher angiogenic activity than low-grade renal cell carcinoma based on histomorphological quantification and qRT–PCR mRNA expression profile. Br J Cancer 2007;96:1888–95. https://doi.org/10.1038/sj.bjc.6603796.
[30] Cheng S-H, Liu J-M, Liu Q-Y, et al. Prognostic role of microvessel density in patients with renal cell carcinoma: a meta-analysis. Int J Clin Exp Pathol 2014;7:5855–63.
[31] Yao J-X, Chen X, Xi W, et al. Immunoscore system for predicting clinical outcome of metastatic renal cell carcinoma patients treated with tyrosine kinase inhibitors. J Cancer 2018;9:4099–107. https://doi.org/10.7150/jca.27408.
[32] Goel S, Duda DG, Xu L, et al. Normalization of the vasculature for treatment of cancer and other diseases. Physiol Rev 2011;91:1071–121. https://doi.org/10.1152/physrev.00038.2010.
[33] López JI, Erramuzpe A, Guarch R, et al. CD34 immunostaining enhances a distinct pattern of intratumor angiogenesis with prognostic implications in clear cell renal cell carcinoma. APMIS 2017;125:128–33. https://doi.org/10.1111/apm.12649.
[34] Budczies J, Klauschen F, Sinn BV, et al. Cutoff finder: a comprehensive and straightforward web application enabling rapid biomarker cutoff optimization. PLoS One 2012;7:e51862. https://doi.org/10.1371/journal.pone.0051862.
[35] Raskov H, Orhan A, Christensen JP, et al. Cytotoxic CD8+ T cells in cancer and cancer immunotherapy. Br J Cancer 2021;124:359–67. https://doi.org/10.1038/s41416-020-01048-4.

[36] Lee JS, Ruppin E. Multiomics prediction of response rates to therapies to inhibit programmed cell death 1 and programmed cell death 1 ligand 1. JAMA Oncol 2019;5:1614–8. https://doi.org/10.1001/jamaoncol.2019.2311.
[37] Nyman J, Denize T, Bakouny Z, et al. Spatially aware deep learning reveals tumor heterogeneity patterns that encode distinct kidney cancer states. Cell Rep Med 2023;4:101189. https://doi.org/10.1016/j.xcrm.2023.101189.
[38] Clark DJ, Dhanasekaran SM, Petralia F, et al. Integrated proteogenomic characterization of clear cell renal cell carcinoma. Cell 2019;179:964–983.e31. https://doi.org/10.1016/j.cell.2019.10.007.
[39] Galon J, Bruni D. Approaches to treat immune hot, altered and cold tumours with combination immunotherapies. Nat Rev Drug Discov 2019;18:197–218. https://doi.org/10.1038/s41573-018-0007-y.
[40] Hegde PS, Karanikas V, Evers S. The where, the when, and the how of immune monitoring for cancer immunotherapies in the era of checkpoint inhibition. Clin Cancer Res Off J Am Assoc Cancer Res 2016;22:1865–74. https://doi.org/10.1158/1078-0432.CCR-15-1507.
[41] Galon J, Mlecnik B, Bindea G, et al. Towards the introduction of the "Immunoscore" in the classification of malignant tumours. J Pathol 2014;232:199–209. https://doi.org/10.1002/path.4287.
[42] Mahmoud SMA, Paish EC, Powe DG, et al. Tumor-infiltrating CD8+ lymphocytes predict clinical outcome in breast cancer. J Clin Oncol 2011;29:1949–55. https://doi.org/10.1200/JCO.2010.30.5037.
[43] Zhang L, Conejo-Garcia JR, Katsaros D, et al. Intratumoral T cells, recurrence, and survival in epithelial ovarian cancer. N Engl J Med 2003;348:203–13. https://doi.org/10.1056/NEJMoa020177.
[44] Nakakubo Y, Miyamoto M, Cho Y, et al. Clinical significance of immune cell infiltration within gallbladder cancer. Br J Cancer 2003;89:1736–42. https://doi.org/10.1038/sj.bjc.6601331.
[45] Li X-D, Huang C-W, Liu Z-F, et al. Prognostic role of the immunoscore for patients with urothelial carcinoma of the bladder who underwent radical cystectomy. Ann Surg Oncol 2019;26:4148–56. https://doi.org/10.1245/s10434-019-07529-y.
[46] Yu A, Mansure JJ, Solanki S, et al. Presence of lymphocytic infiltrate cytotoxic T lymphocyte CD3+, CD8+, and immunoscore as prognostic marker in patients after radical cystectomy. PLoS One 2018;13:e0205746. https://doi.org/10.1371/journal.pone.0205746.
[47] Zhang D, Ni Y, Wang Y, et al. Spatial heterogeneity of tumor microenvironment influences the prognosis of clear cell renal cell carcinoma. J Transl Med 2023;21:489. https://doi.org/10.1186/s12967-023-04336-8.
[48] Chakiryan NH, Kim Y, Berglund A, et al. Geospatial characterization of immune cell distributions and dynamics across the microenvironment in clear cell renal cell carcinoma. J Immunother Cancer 2023;11:e006195. https://doi.org/10.1136/jitc-2022-006195.
[49] Teke K, Yaprak Bayrak B, Yuksekkaya M, et al. Prognostic value of immunological profile based on CD8+ and FoxP3+ T lymphocytes in the peritumoral and intratumoral subsites for renal cell carcinoma. Int Urol Nephrol 2020;52:2289–99. https://doi.org/10.1007/s11255-020-02592-x.
[50] Kishore BK, Robson SC, Dwyer KM. CD39-adenosinergic axis in renal pathophysiology and therapeutics. Purinergic Signal 2018;14:109–20. https://doi.org/10.1007/s11302-017-9596-x.
[51] Bastid J, Regairaz A, Bonnefoy N, et al. Inhibition of CD39 enzymatic function at the surface of tumor cells alleviates their immunosuppressive activity. Cancer Immunol Res 2015;3:254–65. https://doi.org/10.1158/2326-6066.CIR-14-0018.
[52] Drachneris J, Rasmusson A, Morkunas M, et al. CD8+ cell density gradient across the tumor epithelium–stromal interface of non-muscle invasive papillary urothelial carcinoma predicts recurrence-free survival after BCG immunotherapy. Cancers 2023;15:1205. https://doi.org/10.3390/cancers15041205.
[53] Zhang B, Ji H, Yan D, et al. Lack of association of microvessel density with prognosis of renal cell carcinoma: evidence from meta-analysis. Tumour Biol J Int Soc Oncodevelopmental Biol Med 2014;35:2769–76. https://doi.org/10.1007/s13277-013-1367-x.
[54] Iakovlev VV, Gabril M, Dubinski W, et al. Microvascular density as an independent predictor of clinical outcome in renal cell carcinoma: an automated image analysis study. Lab Invest 2012;92:46–56. https://doi.org/10.1038/labinvest.2011.153.
[55] Jasti J, Zhong H, Panwar V, et al. Histopathology based AI model predicts anti-angiogenic therapy response in renal cancer clinical trial. ArXiv 2024. arXiv:2405.18327v1.
[56] Kaneko Y, Masuda T, Takamatsu K, et al. Volumetric imaging of the tumor microvasculature reflects outcomes and genomic states of clear cell renal cell carcinoma. J Pathol Clin Res 2024;10:e12388. https://doi.org/10.1002/2056-4538.12388.
[57] Fang J, Lu Y, Zheng J, et al. Exploring the crosstalk between endothelial cells, immune cells, and immune checkpoints in the tumor microenvironment: new insights and therapeutic implications. Cell Death Dis 2023;14:586. https://doi.org/10.1038/s41419-023-06119-x.
[58] Chen Y, Jin Y, Hu X, et al. Infiltrating T lymphocytes in the tumor microenvironment of small cell lung cancer: a state of knowledge review. J Cancer Res Clin Oncol 2022;148:881–95. https://doi.org/10.1007/s00432-021-03895-x.
[59] Huijbers EJM, Khan KA, Kerbel RS, et al. Tumors resurrect an embryonic vascular program to escape immunity. Sci Immunol 2022;7. https://doi.org/10.1126/sciimmunol.abm6388. eabm6388.
[60] Huang Y, Kim BYS, Chan CK, et al. Improving immune-vascular crosstalkfor cancer immunotherapy. Nat Rev Immunol 2018;18:195–203. https://doi.org/10.1038/nri.2017.145.
[61] Lee YJ, Jeon SH, Yeo JH, et al. Tumor-specific but immunosuppressive CD39+CD8+ T cells exhibit double-faceted roles in clear cell renal cell carcinoma. Cell Rep Med 2025;6:102360. https://doi.org/10.1016/j.xcrm.2025.102360.
[62] Li Y, Wang Z, Jiang W, et al. Tumor-infiltrating TNFRSF9+ CD8+ T cells define different subsets of clear cell renal cell carcinoma with prognosis and immunotherapeutic response. OncoImmunology n.d.;9:1838141. https://doi.org/10.1080/2162402X.2020.1838141.
[63] Leibovich BC, Lohse CM, Cheville JC, et al. Predicting oncologic outcomes in renal cell carcinoma after surgery. Eur Urol 2018;73:772–80. https://doi.org/10.1016/j.eururo.2018.01.005.
[64] Lam JS, Shvarts O, Leppert JT, et al. Renal cell carcinoma 2005: new frontiers in staging, prognostication and targeted molecular therapy. J Urol 2005;173:1853–62. https://doi.org/10.1097/01.ju.0000165693.68449.c3.
[65] EAU guidelines. Edn. presented at the EAU annual Congress Paris 2024. ISBN 978-94-92671-23-3. n.d.
[66] May M, Aziz A, Zigeuner R, et al. Gender differences in clinicopathological features and survival in surgically treated patients with renal cell carcinoma: an analysis of the multicenter CORONA database. World J Urol 2013;31:1073–80. https://doi.org/10.1007/s00345-013-1071-x.
[67] Ning K, Peng Y, Jiang Y, et al. Sex differences in renal cell carcinoma: a single-cell analysis reveals exhausted CD8+ T-cells highly infiltrated in males. Biol Sex Differ 2023;14:58. https://doi.org/10.1186/s13293-023-00540-9.
[68] Thomas AZ, Adibi M, Borregales LD, et al. Surgical management for local retroperitoneal recurrence of renal cell carcinoma after radical nephrectomy. J Urol 2015;194:316–22. https://doi.org/10.1016/j.juro.2015.02.2943.
[69] Psutka SP, Heidenreich M, Boorjian SA, et al. Renal fossa recurrence after nephrectomy for renal cell carcinoma: prognostic features and oncological outcomes. BJU Int 2017;119:116–27. https://doi.org/10.1111/bju.13620.
[70] Itano NB, Blute ML, Spotts B, et al. Outcome of isolated renal cell carcinoma fossa recurrence after nephrectomy. J Urol 2000;164:322–5.
[71] Marchioni M, Sountoulides P, Furlan M, et al. Management of local recurrence after radical nephrectomy: surgical removal with or without systemic treatment is still the gold standard. Results from a multicenter international cohort. Int Urol Nephrol 2021;53:2273–80. https://doi.org/10.1007/s11255-021-02966-9.
[72] Choueiri TK, Tomczak P, Park SH, et al. Overall survival with adjuvant pembrolizumab in renal-cell carcinoma. N Engl J Med 2024;390:1359–71. https://doi.org/10.1056/NEJMoa2312695.
[73] van Delden JJM, van der Graaf R. Revised CIOMS international ethical guidelines for health-related research involving humans. JAMA 2017;317:135–6. https://doi.org/10.1001/jama.2016.18977.